

Beyond diagonal approximations: improved covariance modeling for pulsar timing array data analysis

Marco Crisostomi^{1,2,*}, Rutger van Haasteren^{3,†}, Patrick M. Meyers^{1,‡} and Michele Vallisneri^{4,1§}

¹*TAPIR, California Institute of Technology, Pasadena, CA 91125, USA*

²*Dipartimento di Fisica, Università di Pisa, Largo B. Pontecorvo 3, 56127 Pisa, Italy*

³*Max-Planck-Institut für Gravitationsphysik (Albert-Einstein-Institut), Callinstraße 38, D-30167, Hannover, Germany
Leibniz Universität Hannover, D-30167, Hannover, Germany and*

⁴*Department of Physics, ETH Zürich, Wolfgang-Pauli-Strasse 27, 8093 Zürich, Switzerland*

Pulsar Timing Array (PTA) searches for nHz gravitational-wave backgrounds (GWBs) typically model time-correlated noise by assuming a diagonal covariance in Fourier space, neglecting inter-frequency correlations introduced by the finite observation window. We show that this diagonal approximation can lead to biased estimates of spectral parameters, especially for the common red process that represents the GWB. To address these limitations, we present a method that (i) computes the time-domain autocorrelation on a coarse grid using a fast Fourier transform (FFT), (ii) interpolates it accurately to the unevenly sampled observation times, and (iii) incorporates it into a low-rank likelihood via the Sherman–Morrison–Woodbury identity. Using both analytic covariance comparisons and end-to-end simulations inspired by the NANOGrav 15-year dataset, we demonstrate that our method captures frequency correlations faithfully, avoids Gibbs ringing, and recovers unbiased spectral parameters with modest computational cost. As PTA datasets increase in sensitivity and complexity, our approach offers a practical and scalable path to fully accurate covariance modeling for current and future analyses.

I. INTRODUCTION

Pulsar Timing Arrays (PTAs) provide a unique means to probe gravitational waves (GWs) through the long-term monitoring of the times of arrival (TOAs) of radio pulses from millisecond pulsars [1, 2]. These TOAs can be searched for the imprint of a stochastic gravitational-wave background (GWB, [3]) produced by, for example, an ensemble of astrophysical binary black holes [4], or by relic processes from the early Universe. Given that the GWB effect is weak and easily confused with low-frequency noise, robust detection relies on the cross-correlation of signals from multiple pulsars [5–7], modeled under the assumption that the underlying stochastic process is Gaussian and statistically stationary [8, 9].

A key element in PTA data analysis is the efficient and accurate modeling of the covariance matrix of the timing residuals. In practice, several complicating factors arise that render the task nontrivial: (i) the power spectra of the relevant signals are extremely steep (often following a power law) and are heavily dominated by low-frequency power; (ii) the sampling of the pulsar observations is highly irregular; and (iii) the timing residuals have been pre-processed by projecting out deterministic timing-model components via a least-squares fit. To overcome the computational challenges inherent in directly inverting the full covariance matrix over many thousands of unevenly sampled points, PTA analyses typically employ a low-rank representation of the low-frequency model components, in which covariance is

expanded in a Fourier basis. In the standard formulation the Fourier-space covariance is taken to be diagonal (i.e., no frequency correlations are included), an approximation that is well motivated [10–14] but that may not be accurate enough and could introduce biases in the inference of spectral parameters.

In this work we develop an improved method to model the full frequency-correlated covariance matrix. Our approach combines the efficiency of a rank-reduced representation with the fidelity of direct time-domain methods, by employing the fast Fourier transform (FFT) and a localized interpolation scheme. Our proposed method not only accounts for the intrinsic correlations induced by finite-window effects (or equivalently by approximating Fourier integrals as Fourier series), but also mitigates Gibbs ringing artifacts inherent in any Fourier-based approach when severely reducing the number of frequency modes. In Sec. II we review the traditional Fourier-sum approach and then introduce our new method. In Sec. III we compare the performance of various covariance approximations. In Sec. IV we apply our method to simulated PTA datasets inspired by the NANOGrav 15-yr data release. In Sec. V we offer our conclusions.

We have implemented the methods discussed in this paper in the *Enterprise* [15] and *Discovery* [16] PTA data-analysis packages. Most of our results were produced using *Discovery*, exploiting its JAX-based [17] autodifferentiation [18] to sample Bayesian posteriors using Hamiltonian Monte Carlo, in the “No-U-Turn” implementation [19] of NumPyro [20, 21].

* mcrisost@caltech.edu

† rutger@vhaasteren.com

‡ pmeyers@caltech.edu

§ mvallisneri@ethz.ch

II. COVARIANCE MATRICES IN PTA DATA ANALYSIS

In PTA data analysis, the timing residuals $\delta\mathbf{t}$ (i.e., the differences between the measured and expected TOAs, as predicted by a deterministic *timing model*) are described as arising from a combination of white measurement noise and one or more time-correlated processes. In many instances the correlated processes (e.g., intrinsic pulsar spin noise or the common GWB signal) are assumed to be Gaussian and stationary. Although any complete basis can be used to develop their low-rank representation, traditionally these processes are described in either the time domain or the Fourier domains. In this section we summarize the theory of Gaussian-process covariance, we describe its standard Fourier-domain formulation, and we introduce our new method.

A. Time-series modeling of stationary processes

Let $y(t)$ denote a real zero-mean stationary random process

$$\langle y(t) \rangle = 0, \quad (1)$$

with autocorrelation function [22]

$$\langle y(t) y(t') \rangle \equiv C(|t - t'|), \quad (2)$$

which depends solely on the time-lag $\tau = |t - t'|$. By the Wiener–Khinchin theorem, the autocorrelation function is the Fourier transform of the two-sided power spectral density (PSD) $\mathcal{S}(f)$:

$$C(\tau) = \int_{-\infty}^{+\infty} df \mathcal{S}(f) e^{i2\pi f\tau}. \quad (3)$$

The two-sided PSD $\mathcal{S}(f)$ is defined for $-\infty < f < +\infty$ with $\mathcal{S}(-f) = \mathcal{S}(f)$. In the Fourier domain the same process is represented as

$$\langle \tilde{y}(f) \rangle = 0, \quad (4)$$

with

$$\langle \tilde{y}(f) \tilde{y}^*(f') \rangle = \mathcal{S}(f) \delta(f - f'), \quad (5)$$

where the Fourier transform of $y(t)$ is defined in the usual way:

$$\tilde{y}(f) = \int_{-\infty}^{+\infty} dt y(t) e^{-i2\pi ft}. \quad (6)$$

Expanding $y(t)$ in a complex Fourier series over the finite time interval $t \in [-T/2, T/2]$, we write

$$y(t) = \sum_{k=-\infty}^{+\infty} \tilde{y}^k e^{i2\pi f_k t}, \quad (7)$$

where the discrete frequencies are given by $f_k = k/T$. The Fourier coefficients can be obtained via

$$\tilde{y}^k = \frac{1}{T} \int_{-T/2}^{T/2} dt y(t) e^{-i2\pi f_k t}. \quad (8)$$

From these definitions the Fourier-domain covariance (or the power in each Fourier bin) follows as

$$\begin{aligned} S_{jk} &\equiv \langle \tilde{y}^j \tilde{y}^{k*} \rangle \\ &= \frac{1}{T^2} \int_{-T/2}^{T/2} dt \int_{-T/2}^{T/2} dt' C(|t - t'|) e^{-i2\pi f_j t} e^{i2\pi f_k t'}. \end{aligned} \quad (9)$$

Using the Wiener–Khinchin theorem with Eq. (5), this double time integral can be re-expressed as an integral over frequency:

$$S_{jk} = \int_{-\infty}^{+\infty} df \mathcal{S}(f) \text{sinc}[\pi T(f - f_j)] \text{sinc}[\pi T(f - f_k)], \quad (10)$$

where $\text{sinc}(x)$ denotes the cardinal sine function $\sin(x)/x$. Equation (10) demonstrates that, even for a stationary process, the Fourier coefficients defined over a finite interval are not strictly uncorrelated but rather display correlations mediated by the sinc functions. Now, in current PTA analyses the covariance is typically approximated in the diagonal form

$$S_{jk} \propto \mathcal{S}(f_j) \delta_{jk}, \quad (11)$$

which neglects these inter-frequency correlations. In what follows we show that this diagonal approximation may induce systematic biases, motivating the development of improved computational methods that fully capture the frequency correlations.

B. Standard method: Fourier sum

PTA datasets consist of a large number of pulsar-timing residuals $\delta\mathbf{t}$ observed at unevenly spaced times. The $\delta\mathbf{t}$ are produced by subtracting a best-fit theoretical model from the TOAs [23]. The residuals are modeled as the sum of a number of Gaussian noise processes: these may have independent probability distributions for each residual, or they may be correlated across TOAs (the former are usually called “white noise,” reserving the term “Gaussian processes” for the latter). If a time-correlated Gaussian process, such as intrinsic spin noise or the GWB, is also stationary, it is fully described by the autocorrelation function of the residuals $C(\tau)$, which is related to the PSD by the Wiener–Khinchin theorem of Eq. (3). In standard PTA analyses, it is customary to work with the one-sided PSD

$$S(f) = \begin{cases} 2\mathcal{S}(f), & f > 0, \\ 0, & f < 0, \end{cases} \quad (12)$$

so that all the power resides at positive frequencies. With this convention

$$C(\tau) = \int_0^{+\infty} df S(f) \cos(2\pi f\tau). \quad (13)$$

In the rest of this paper we will work with the one-sided PSD $S(f)$. If $S(f)$ diverges sufficiently strongly for $f \rightarrow 0$, as is the case for a power law $\propto f^{-\gamma}$ with $\gamma \geq 1$, the integral of Eq. (13) is divergent, requiring the introduction of a low-frequency cutoff or regularization. For a generic power law, this results in a time-domain power law $\propto \tau^{\gamma-1}$ corrected by a hypergeometric function [22]. For power-law PSDs with $\gamma < 1$ the integral diverges as $f \rightarrow \infty$ and a high-frequency cutoff or regularization is needed.

The PTA log likelihood can be written in general as

$$\begin{aligned} \log p(\delta\mathbf{t}|\Lambda) = & -\frac{1}{2}(\delta\mathbf{t} - M\boldsymbol{\epsilon})^T [N + C(\Lambda)]^{-1} (\delta\mathbf{t} - M\boldsymbol{\epsilon}) \\ & - \frac{1}{2} \log |2\pi [N + C(\Lambda)]|, \end{aligned} \quad (14)$$

where M is a design matrix given by the derivatives of the deterministic model with respect to the model parameters (e.g., the spin period and period derivative of the neutron star), and the $\boldsymbol{\epsilon}$ are linear corrections to those parameters; N is the covariance matrix of white (measurement) noise; C is the sum of the Gaussian-process covariance matrices, which are functions of the noise hyperparameters Λ . As written here, C is a large dense matrix, so computing its inverse is impractical for real datasets. Furthermore, the elements of C may themselves be too expensive to compute or numerically unstable, as is the case for the hypergeometric function.

Instead, finite Gaussian-process bases are used to reduce the dimensionality of the problem and evaluate the likelihood more efficiently [9, 10, 22, 24–26]. To wit, Gaussian processes are written as the product of a basis F and weights \mathbf{a} , which follow a Gaussian prior. So the PTA log likelihood may be written (omitting the timing model corrections for the moment)

$$\begin{aligned} \log p(\delta\mathbf{t}|\mathbf{a}) = & -\frac{1}{2}(\delta\mathbf{t} - F\mathbf{a})^T N^{-1} (\delta\mathbf{t} - F\mathbf{a}) \\ & - \frac{1}{2} \log |2\pi N|, \end{aligned} \quad (15)$$

with

$$\log p(\mathbf{a}|\Lambda) = -\frac{1}{2}\mathbf{a}^T \Phi^{-1}(\Lambda)\mathbf{a} - \frac{1}{2} \log |2\pi \Phi(\Lambda)|, \quad (16)$$

and marginalizing $p(\delta\mathbf{t}|\mathbf{a})p(\mathbf{a}|\Lambda)$ over the weights \mathbf{a} ,

$$\begin{aligned} \log p(\delta\mathbf{t}|\Lambda) = & -\frac{1}{2}\delta\mathbf{t}^T [N + F\Phi(\Lambda)F^T]^{-1} \delta\mathbf{t} \\ & - \frac{1}{2} \log |2\pi [N + F\Phi(\Lambda)F^T]|. \end{aligned} \quad (17)$$

While the matrix $N + F\Phi F^T$ is still large, it can be inverted using the Woodbury lemma,

$$\begin{aligned} [N + F\Phi(\Lambda)F^T]^{-1} = & N^{-1} \\ & - N^{-1}F(\Phi^{-1} + F^T N^{-1}F)^{-1}F^T N^{-1}; \end{aligned} \quad (18)$$

this expression is much more computationally efficient since N is usually diagonal (or almost), and the inner inverses in (18) have the dimension of the number of bases, which is much smaller than the number of residuals (a few tens vs. tens of thousands). We can perform a similar marginalization process for the timing-model corrections $\boldsymbol{\epsilon}$, usually by adopting a broad, uninformative prior. We discuss the effect of timing-model marginalization on the low-rank reconstruction of C in Sec. III.

Beginning with Ref. [24], PTA analyses have used Fourier bases for this low-rank representation: the \mathbf{a} are Fourier coefficients for frequencies $f_k = k/T$, with T the total observation time and $k = 1, \dots, n$; and F is a discrete Fourier transform matrix of sines and cosines, albeit evaluated at unequally spaced times. Comparing Eqs. (14) and (17), we see that the full C is approximated as $F\Phi F^T$, so

$$\begin{aligned} C_{ab} \approx \sum_{j,k=1}^n \Phi_{jk} [\cos(2\pi j t_a/T) \cos(2\pi k t_b/T) \\ + \sin(2\pi j t_a/T) \sin(2\pi k t_b/T)] . \end{aligned} \quad (19)$$

The main issue here is that, up through the recent GWB “evidence-for” articles [27–31], the Gaussian-process prior is set from Eq. (11): $\Phi_{jk} = S(j/T)\delta_{jk}$, neglecting the inter-frequency correlations of Eq. (10). In Sec. IV we will see that these correlations have measurable consequences on parameter estimation. Furthermore, a diagonal Φ_{jk} corresponds to a periodic correlation function (with $C(0) = C(T)$), which is obviously wrong for the physical noise processes of interest, as noted already in [10].

While it may seem that this problem could be solved by using Eq. (19) and taking Φ_{jk} from Eq. (10), doing so poses further problems. First, Eq. (19) is then effectively a two-dimensional Fourier series over a finite domain, which will suffer from Gibbs ringing artifacts near its boundaries [32, 33], slowing the convergence of the expansion; we will explore this numerically in Sec. III. Second, Eq. (10) requires performing a highly oscillatory integral that is both delicate numerically and computationally expensive.

C. New method: Wiener–Khinchin by FFT + linear interpolation

In this section we introduce a novel method to approximate the full covariance matrix efficiently and accurately without performing the computationally intensive double-sinc integral of Eq. (10). Our method relies

on evaluating the time-domain autocorrelation function $C(\tau)$ on a coarse time grid using a fast Fourier transform of the PSD, thus retaining the frequency-correlation information that is lost in the diagonal approximation of Eq. (11). The coarse-time covariance matrix is then interpolated efficiently to the full set of TOAs, with the additional advantage that the locally concentrated interpolation basis mitigates finite-window effects and artifacts arising from the periodic boundary conditions implicitly assumed in the Fourier-basis approach.

For a stationary Gaussian process, the time-domain covariance matrix for a set of regularly spaced times has the *Toeplitz* structure, where each descending diagonal is set to the value of the autocorrelation function for the corresponding lag. That is, if $C_{ab} = C(|t_a - t_b|)$ with $t_a = a\Delta t$ and $a = 1, \dots, N$, then the main diagonal C_{aa} would be set to $C(\tau = 0)$; the super- and sub-diagonals $C_{a,a\pm 1}$ would be set to $C(\tau = \Delta t)$, and so on. This means that the full covariance matrix can be recovered from the vector $c_a = C(a\Delta t)$, which we will compute using the fast Fourier transform.

Furthermore, for noise processes dominated by the lowest frequencies (as are those of interest in PTA data analysis), the autocorrelation function varies smoothly, which makes it possible to represent it on a coarse time grid and then interpolate to every TOA. The resulting covariance matrix can be written as $B\hat{C}B^T$, where \hat{C} is the coarse-timescale covariance matrix, and the interpolation matrix B has a locally concentrated structure set by the interpolation order (for linear interpolation, which we use throughout unless otherwise specified, it would consist of the sum of “hat” functions for each pair of coarse times, evaluated at the TOAs; see, e.g., [34]). This $B\hat{C}B^T$ can be inserted directly in Eq. (17) as a replacement for $F\Phi F^T$.

Last, we compute the coarse-time autocorrelation vector \hat{c}_a by evaluating the Wiener–Khinchin integral (13) as the Fourier sum

$$\begin{aligned}\hat{c}_a &\approx \Delta f \sum_{k=0}^{n_{\max}-1} S(f_k) \cos(2\pi f_k \tau_a) \\ &= \Delta f \sum_{k=0}^{n_{\max}-1} S(k \Delta f) \cos(2\pi a k \Delta \hat{t} \Delta f),\end{aligned}\quad (20)$$

where $\Delta f = 1/(\omega T)$, with ω an integer *oversampling factor*; $\Delta \hat{t}$ is the spacing of coarse times; and n is chosen such that $n_{\max} \Delta f \approx \zeta/(2\Delta \hat{t})$ (i.e., we integrate to ζ times the Nyquist frequency of the coarse time grid). Setting $\omega > 1$ increases the frequency resolution, while $\zeta > 1$ ensures that higher frequencies are included in the Wiener–Khinchin integral.

We evaluate Eq. (20) using the inverse fast cosine transform, which results in a vector of length¹ $2\zeta\omega n$; \hat{c}_a is then given by every ζ -th element of the transform, for the first $\hat{N} = 2n+1$ elements. This procedure ensures the

accurate and efficient evaluation of the Wiener–Khinchin integral and allows for a controlled trade-off between computational cost and accuracy by choosing ω and ζ . When analyzing an array of pulsars together, the same coarse time basis and covariance matrix can be shared among them, as long as T is set to the total time span of the multipulsar dataset, and the appropriate matrix B_i is used for each pulsar.

III. COMPARISON OF METHODS

In this section, we compare the true full-rank time-domain covariance matrix with the three low-rank reconstructions discussed above.

A. Comparing covariance matrices for Matérn covariance function

For this comparison, we study a numerically well-behaved PSD that is low-frequency-dominated and sufficiently similar to that signals that appear in PTA models. Namely, we focus on *Matérn* process of order $3/2$, which has PSD

$$S_{3/2}(f) = \frac{24 \sqrt{3} \lambda \sigma^2}{\left[(2\pi \lambda f)^2 + 3\right]^2}, \quad (21)$$

where λ is the length scale of the process and σ the variance. Note that $S_{3/2}(f)$ goes to a constant as $f \rightarrow 0$ and vanishes as f^{-4} for $f \rightarrow \infty$. Thus $C(\tau)$ is always well defined. The corresponding correlation function is given by integrating $S_{3/2}(f)$ in Eq. (13):

$$C_{3/2}(\tau) = \frac{\sigma^2 (\lambda + \sqrt{3}\tau) e^{-\frac{\sqrt{3}\tau}{\lambda}}}{\lambda}. \quad (22)$$

For easy reference, we name the four methods under consideration:

- **TRUECOVARIANCE**: the exact covariance matrix given by Eq. (22);
- **DIAGONALPHI**: the low-rank approximation $F\Phi F^T$ with diagonal Φ set from Eqs. (11) and (21);
- **SINCPHI**: the low-rank approximation $F\Phi F^T$ with a non-diagonal Φ computed from Eqs. (10) and (21);
- **FFTINT**: our new approximation $B\hat{C}B^T$.

In the top row of Fig. 1 we show these covariance matrices for an evenly spaced series of 2001 observation times for a time window T between $t_{\text{in}} = 2000$ and $t_{\text{fin}} = 6000$ (in arbitrary dimensionless units). We set $\lambda = 2000$ and $\sigma = 1$; we take $n = 60$ for **DIAGONALPHI** and **SINCPHI**; and, to cover the same frequency band, we use $\hat{N} = 121$

¹ For efficiency, our implementation requires $\omega > 1$.

Reconstruction	$ \overline{\Delta C} $	$ \overline{\Delta C_P} $
DIAGONALPHI	0.46	$2.3 \cdot 10^{-3}$
SINCPHI	$4 \cdot 10^{-3}$	$5.5 \cdot 10^{-4}$
FFTINT	$3 \cdot 10^{-5}$	$1.8 \cdot 10^{-5}$

TABLE I. Average element-wise absolute difference between the exact and low-rank-approximated Matérn_{3/2} covariance matrices, shown pre ($|\overline{\Delta C}|$) and post ($|\overline{\Delta C_P}|$) quadratic projection.

coarse grained times for FFTINT, with $\omega = 6$ and $\zeta = 1$, for a total of 361 FFT frequencies. This comparison shows that DIAGONALPHI is a very inaccurate approximation to TRUECOVARIANCE, even for the main diagonal (which is equal to $C(0)$), while SINCPHI and FFTINT appear to be much closer. This happens because for DIAGONALPHI $C(0) = T^{-1} \sum_k S(f_k)$, while SINCPHI and FFTINT embody more accurate representations of the Wiener-Khinchin integral that can access the value of $S(f)$ between “bin” frequencies k/T .

However, comparing the matrices in this fashion is not entirely relevant to PTA data analysis. In the bottom row of Fig. 1 we show the same covariance matrices after projecting out the subspace of residuals orthogonal to the family of generic quadratic functions of the TOAs. Doing so mimics the most significant effects of marginalizing the PTA likelihood over timing-model errors, which is standard practice for PTAs [25]. The projected covariance matrix is $C_P \equiv PCP^T$, where the projector $P = I - M(M^T M)^{-1}M^T$, and M is a *design matrix* with columns given by constant, linear, and quadratic functions of the TOAs. The projection reduces differences significantly. This can be partly understood by observing that the Fourier basis is strictly periodic with period $1/T$, which means that the first and last observations in the time-domain have the same response. The presence of a constant and linear basis in M breaks that symmetry, and allows the approximation to more accurately follow the model.

The absolute element-wise differences $|\Delta C|$ between TRUECOVARIANCE and the approximated covariances are plotted in Fig. 2 (post projection), and summarized in Table I, which shows the matrix-averaged difference pre and post projection. Although the four matrices at the bottom of Fig. 1 look very similar, the DIAGONALPHI errors remain much larger, and SINCPHI gets in trouble at the edges of the matrix, with the Gibbs phenomenon apparent in the dense regular pattern of high-error “dots.” By contrast, FFTINT remains very accurate across all TOA pairs.

In Appendix B we investigate the accuracy of the different covariance approximations on a family of Gaussian PSDs. The Gaussian PSDs form an over-complete basis, and as such any well-behaved PSD can be accurately decomposed in some sum of these Gaussian PSDs. We find results similar in nature to the results in this section.

B. Convergence of the covariance function

Next, we are interested in how the low-rank approximation of the covariance matrix converges to the true covariance matrix as a function of approximation parameters \hat{N} , ω , and ζ . As in Sec. III A, we focus on the Matérn PSD, but we also study a pure power-law PSD.

In the PTA literature, power-law signals are typically parameterized as

$$S_{\text{PL}}(f) = \frac{A^2}{12\pi^2 f_{\text{ref}}^3} \left(\frac{f}{f_{\text{ref}}} \right)^{-\gamma}, \quad (23)$$

where $f_{\text{ref}} = 1 \text{ yr}^{-1}$, A is the amplitude of the noise process at f_{ref} , and γ is the positive spectral index. Power-law signals are problematic from a theoretical point of view, because the total power represented by such a signal is infinite: for $\gamma \geq 1$ the power diverges as $f \rightarrow 0$, while for $\gamma \leq 1$ the total power diverges as $f \rightarrow \infty$. Nevertheless, power-law signals are still used in PTA practice, because the timing model absorbs the $f = 0$ divergence when $1 < \gamma < 7$, while the low-rank approximation sets a high-frequency cutoff. It remains unphysical to consider $\gamma \in [0, 1]$ or $[7, 10]$.

For our convergence study, it is necessary to incorporate a “break” in the power law (i.e., a change in spectral slope) so that we avoid the divergence of total power. This can be done as follows:

$$S_{\text{BPL}}(f) = S_{\text{PL}}(f) \left[1 + \left(\frac{f}{f_b} \right)^{\frac{1}{\kappa}} \right]^{\kappa(\gamma - \delta)}, \quad (24)$$

where κ parametrizes the smoothness of the transition, f_b is the break frequency, and γ (or δ) is the spectral slope when f is sufficiently below (above) f_b . For this convergence study we set $\kappa = 1/2$, $f_b/f_{\text{ref}} = 1/50$, $\gamma = 0$, and $\delta = 13/3$. The choice of $\gamma = 0$ causes the PSD to be flat for $f \rightarrow 0$, while $\delta = 13/3$ sets the slope to a typical steep power law for $f > f_b$. For the Matérn PSD of Eq. (21) we set $\lambda = T$. The amplitudes σ and A for the Matérn process and the broken power law are set so that TRUECOVARIANCE has unit diagonal.

In Fig. 3 we explore how FFTINT covariance matrices converge as we increase \hat{N} and ω . For the comparisons on the left we project out a constant², while on the right we project out a generic quadratic. We find that ζ has a very small effect (except when \hat{N} is obviously too small), so we always set $\zeta = 1$. Convergence is approximately quadratic in \hat{N} until it saturates at a value that decreases with ω ; convergence is also helped by the quadratic projection.

² This is reasonable since the absolute time reference of TOAs is always arbitrary in PTA data analysis.

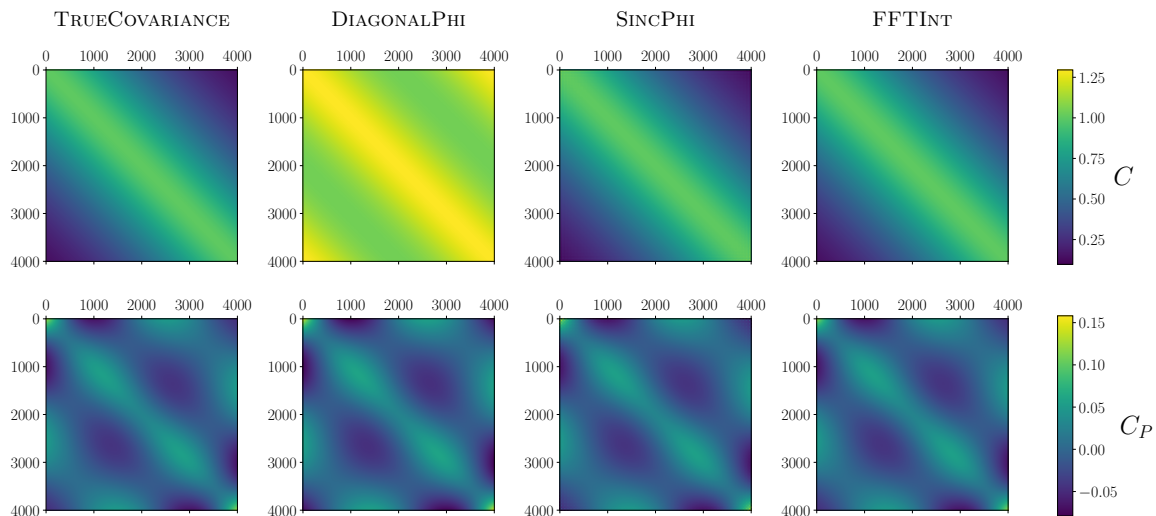


FIG. 1. **Top:** Matérn_{3/2} covariance matrices according to the TRUECOVARIANCE (exact), DIAGONALPHI, SINCPhi, and FFTINT methods. The descending-diagonal Toeplitz structure is evident for all. DIAGONALPHI stands apart because the diagonal kernel makes it periodic. **Bottom:** quadratic-projected covariance matrices C_P . The projection creates an obvious multipolar structure and reduces the differences between the four matrices. Note the reduced range of the color scale.

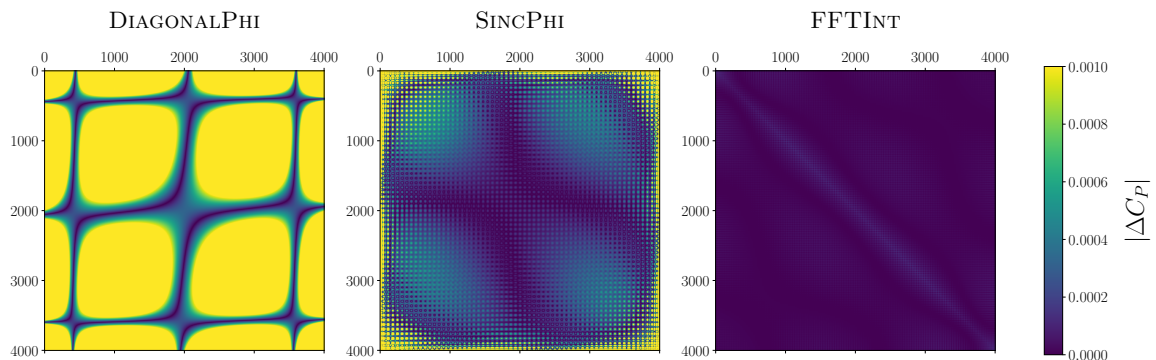


FIG. 2. Element-wise absolute difference between the exact and low-rank-approximated Matérn_{3/2} covariance matrices, shown here after projecting out generic quadratic functions. Note that the “pixelated” structure of the SINCPhi method is real: it is a manifestation of the Gibbs phenomenon that can also be seen in Fig. 4, and it is more pronounced at the edges of the time window.

C. Rank-Reduced Signal Reconstruction and Upsampling

Figure 4 illustrates the impact of our rank-reduced representations on the reconstruction of a stochastic low-frequency signal, and highlights the differences that arise when we upsample the reduced representation. In this example, we begin with a *true* signal generated on a finely sampled grid comprising $N = 10\,000$ evenly spaced time points over the interval $x \in [0, 8\,000]$. This smoothly varying waveform is plotted in blue. We then define the *observation window* as the interval $x_{\text{obs}} \in [2\,000, 6\,000]$, which is indicated by vertical dashed lines in the figure. Although the underlying physical process extends over the full fine grid, we restrict PTA observations to this

sub-interval; this distinction becomes crucial when comparing different reconstruction methods.

For the rank reduction we adopt both the FFT-Interpolation (FFTINT) and the Fourier (SINCPhi) methods. In our implementation we select $\hat{N} = 61$ regularly spaced nodes within the observation window. This choice corresponds to a reduced Fourier basis with $n = 30$ frequency modes. On the coarse-grained grid, the basis is complete—meaning that any signal defined on the nodes can be represented exactly either in the time domain or in the Fourier domain (via an invertible Fourier transform). The “data” in this reduced basis is the true signal subsampled on the node positions \hat{x} to obtain the corresponding values \hat{y} ; these values (shown as orange dots in the figure) are equivalently represented in the Fourier domain

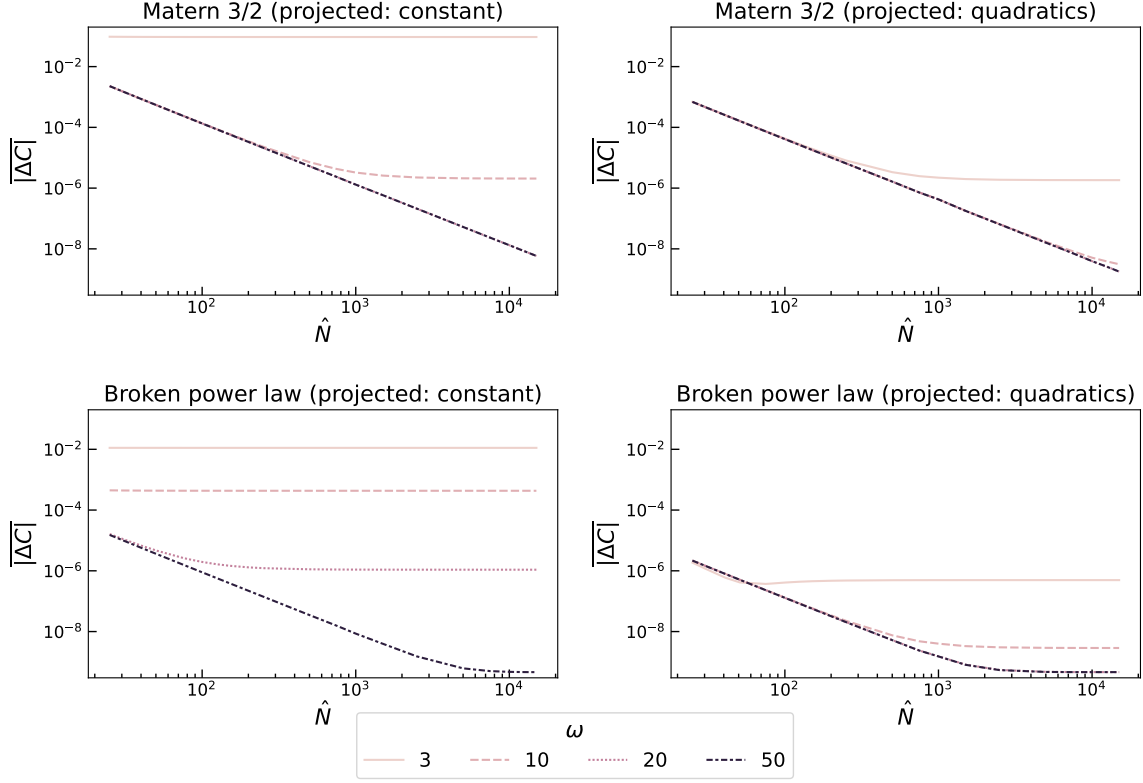


FIG. 3. Mean absolute element-wise difference of the approximated and true covariance matrix as a function of the number of coarse timestamps \hat{N} and the oversampling factor ω for the Matérn_{3/2} and broken power-law kernels. All amplitudes are normalized such that the true (unprojected) covariance matrix is unity on the diagonal.

Top left: Matérn_{3/2} kernel [Eq. (22) with $\lambda = T$]. We project out a constant TOA reference time.

Top right: Same as top left, except we project out a generic quadratic function.

Bottom left: Same as top left, but for the broken power law of Eq. (24), with $\kappa = 1/2$, $f_b = f_{\text{ref}}/50$, $\gamma = 0$, $\delta = 13/3$. We project out a constant TOA reference time.

Bottom right: Same as bottom left, except we project out a generic quadratic function.

by the coefficients a_{SincPhi} . Importantly, on the node grid the FFTINT and the non-diagonal Fourier SINCPhi approaches yield identical results: they cross at the orange dots. We use this time-series 1D approach instead of a 2D covariance approach to illustrate differences between the methods because this is easier to visualize. The same principle applies to the covariance matrices; see Eq. (9).

Once the reduced representation is fixed, we upsample the signal back to the full fine grid. In our FFTINT approach the reconstruction is carried out in the time domain by applying the locally concentrated interpolation matrix B to the coarse signal, yielding an orange dashed line that follows the original blue signal with high fidelity and without artifacts. In contrast, the upsampling in the Fourier representation proceeds by defining the Fourier basis over the same frequencies derived from \hat{x} but evaluating the basis functions on the full fine grid. This procedure leads to the green curve in Fig. 4. Owing to the inherent non-locality of the Fourier basis, the green reconstruction exhibits the well-known Gibbs phenomenon—a ringing artifact that is particularly pronounced at the

edges of the observation window and persists over the entire domain. Interestingly, the Gibbs phenomenon and apparent edge discontinuity also shows up when we draw realizations from the SINCPhi model, such as represented by the middle-right panel of Figure 1.

The inset in Fig. 4 zooms into a representative region of the signal, clearly showcasing the ringing effect in the Fourier-based reconstruction. This comparison demonstrates that, while both representations are exact on the reduced node grid, only the FFTINT method provides a robust and physically motivated upsampling procedure that avoids the spurious oscillations associated with the Fourier approach.

The poor performance of SINCPhi at the extremes of the dataset is clearly visible also in Fig. 2 where the absolute difference is maximum at the edges of the covariance matrix. Note that while the Gibbs phenomenon does not affect the coarse time basis, it will definitely affect the unevenly spaced TOAs found in real PTA datasets.

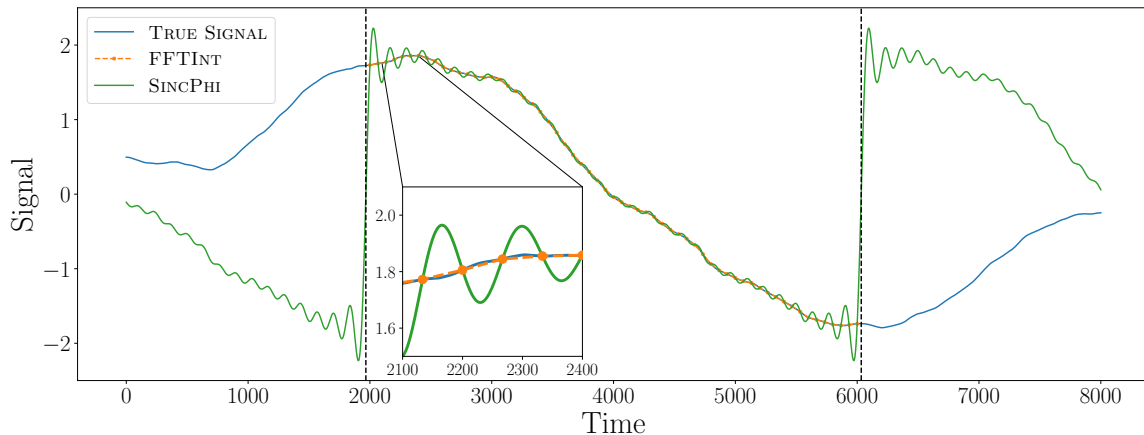


FIG. 4. Comparison of signal reconstruction with time- and frequency-domain bases. The blue curve depicts the “true” stochastic signal generated on a fine grid with 10 000 points over the interval $x \in [0, 8000]$, with an observation window $x \in [2000, 6000]$. The signal, as subsampled on a reduced set of $\hat{N} = 61$ evenly spaced node points (orange dots), with first observation at $x = 2000$ and last observation at $x = 6000$, is represented exactly in both the SINCPhi Fourier and FFTINT interpolation bases. When upsampled to the fine grid, the reconstruction via the interpolation basis (orange dashed line) recovers the true signal accurately, whereas the Fourier-based reconstruction (green curve) exhibits significant ringing due to the Gibbs phenomenon. The inset highlights this ringing effect near the boundaries of the observation interval. The vertical dashed lines, half a timestep before $x = 2000$ and after $x = 6000$, delimit the periodicity implied by the Fourier transform. See Appendix A for an explanation why the periodicity is not exactly equal to the observation window. The FFTINT method provides a robust and physically motivated upsampling procedure that avoids the spurious oscillations associated with the Fourier approach.

IV. PTA ANALYSIS

In this section we compare our new method (FFTINT) to the standard diagonal-covariance formulation (DIAGONALPHI) in the analysis of a simulated dataset inspired by the NANOGrav 15-yr data [23]. The simulation is obtained by setting the pulsar white-noise parameters as in the NANOGrav dataset, and the red-noise parameters in the vicinity of their maximum-likelihood values in the NANOGrav data release. Red noise is generated in the time domain using the FFTINT covariance matrix to color and correlate independent Gaussian samples. The 15-yr TOAs have an uneven cadence $\gtrsim 2$ weeks, so we adopt a coarse-grained timescale of $\hat{N} = 501$ nodes, which yields $\Delta\hat{t} \simeq 12$ days and a Nyquist frequency of $250/T$ Hz, where T is the time span of the dataset (~ 16 years). The oversampling factor ω is 50. We expect these values to guarantee a very accurate simulation indistinguishable from what could be achieved with TRUECOVARIANCE. We model each pulsar’s intrinsic spin noise with the two-parameter power law of Eq. (23). We also include a common spatially uncorrelated red-noise process (which represents the GWB), which follows the broken power law of Eq. (24), with $\kappa = 0.1$.

In the NANOGrav 15-yr GWB analysis [27, 35], this model was used with $\delta = 0$ (a flat tail) to determine the break frequency f_b where red noise is overtaken by white measurement noise. Continuing the red-noise

power law beyond that break leads to an unphysical correlation of white- and red-noise parameters. In the main NANOGrav analysis, spatially correlated red noise was then modeled with a simple power law with a hard cut at f_b . Both prescriptions lead to the same GWB posteriors. In this article however we wish to explore the impact of covariance-matrix approximations on the determination of f_b , so we adopt Eq. (24) with $\delta = 1/3$ —a mildly sloping tail to reduce the injection of power at higher frequencies.

We sample $\log_{10} A_p$ and γ_p for each pulsar p and $\log_{10} A_{\text{gw}}$, γ_{gw} and $\log_{10} f_b$ for the common process. For a dataset of 67 pulsars this gives a total of 137 parameters to estimate. We first explore how the likelihood converges as we increase \hat{N} and ω for the FFTINT method and the number of frequency bins n for the DIAGONALPHI method. For the same frequency content, \hat{N} and n are related by $\hat{N} = 2n + 1$, so when we study the DIAGONALPHI likelihood as a function of \hat{N} , we are computing it for $n = (\hat{N} - 1)/2$. In Fig. 5 we show the difference $\Delta \log L$ for the full PTA likelihood (left and middle) and for three representative pulsars (right) as we vary ω (for FFTINT) and \hat{N} . Differences are computed with respect to FFTINT with $\omega = 2$ (left), and to the minimum between FFTINT and DIAGONALPHI at $\hat{N} = 61$ (middle and right). Since $\Delta \log L$ is essentially constant for $\omega \geq 5$, we use that value in the middle and right plots (and all subsequent analyses). In the central panel we show how the two likelihoods converge as a function of \hat{N} : DIAGO-

NALPHI reaches its plateau at $n \simeq 90$, whereas FFTINT does so at $\hat{N} \simeq 251$. The variations for the larger \hat{N} seem to be explained by shallow-spectrum ($\gamma < 1$) pulsars such as J1022+1001, while red-spectrum ($\gamma > 4$) pulsars such as B1937+21 and intermediate cases such as J1802–2124 are modeled well with smaller \hat{N} . Nevertheless, it appears that relatively large \hat{N} may be needed to fully capture the variation of the NANOGrav PTA.

In Fig. 6 we show the posteriors for the intrinsic red-noise parameters of the three representative pulsars, as estimated as part of the full PTA analysis. The first two rows explore the convergence of posteriors with increasing \hat{N} for DIAGONALPHI and FFTINT. The third row compares the two approximations with $\hat{N} = 251$ ($n = 125$). For both methods, very red spectra (e.g., B1937+21’s) are easily captured even with the smallest number of coarse-time nodes and frequency bins; for milder spectra (e.g., J1802–2124’s) more nodes and bins are needed to improve the accuracy of inference; and for very shallow spectra (e.g., J1022+1001’s) values $\hat{N} = 61$ and $n = 30$ are not sufficient to recover the injection, with progressive improvements with larger values. Overall, for sufficient large \hat{N} and n the two methods agree on intrinsic red-noise parameters.

The situation is quite different for the common red-noise process. In Fig. 7 we show γ_{gw} , $\log_{10} A_{\text{gw}}$, and $\log_{10} f_b$ posteriors, organized in a manner similar to Fig. 6. For DIAGONALPHI, the number of frequency bins has no impact on the estimation of γ_{gw} and A_{gw} , but it does for the break frequency f_b . For FFTINT all posteriors change with \hat{N} . The most important result is illustrated in the third row of Fig. 7: the DIAGONALPHI method is biased in all three parameters, preferring a larger break frequency, smaller spectral index, and larger amplitude.

To understand the origin of this bias for common red-noise process but not for intrinsic pulsar timing noise, we perform another simulation, identical to our first except that we inject only the common noise process. We have only three parameters to infer and we use $\hat{N} = 251$ and $n = 125$. We repeat the analysis with an increasing number of array pulsars n_{psr} . Common red-noise posteriors are shown in Fig. 8 for DIAGONALPHI (first row) and FFTINT (second row) for increasing n_{psr} , and are compared between the two methods for $n_{\text{psr}} = 5$ (third row) and $n_{\text{psr}} = 67$ (the full array, fourth row). It appears that the difference between DIAGONALPHI and FFTINT is subtle enough that the bias emerges only as more and more pulsars are analyzed together.

V. CONCLUSIONS

GWB searches with PTAs rely critically on the accurate modeling of the Gaussian-process covariance of signal and noises alike. In this paper we have shown evidence that the standard approximation (low-rank Fourier reconstruction with a diagonal Fourier-domain prior)

overlooks important frequency correlations induced by the finite observation window, and results in biased parameter estimation. We have described a more refined formulation of covariance, achieved through the application of the fast Fourier transform combined with a localized interpolation scheme, which allows us to efficiently approximate the true covariance matrix while avoiding Gibbs artifacts.

We demonstrated the limitations of the diagonal approximation by comparing it to our new method in targeted analytical tests (Sec. III) and through the analysis of a simulated dataset inspired by the NANOGrav 15-year data release (Sec. IV). The diagonal approximation induces small errors in the estimation of individual-pulsar timing-noise, but it can lead to measurable bias for the parameters of a common red-noise process. Specifically, $\log_{10} A_{\text{gw}}$ is overestimated and γ_{gw} underestimated using DIAGONALPHI. This seems especially important given that the estimates of these parameters from the latest PTA datasets are in tension with theoretical predictions (see, e.g., [27]).

Moreover, as datasets grow in size and sensitivity (by consolidating data from multiple PTAs and with next-generation telescopes such as the SKA), the tolerance for mismodeling will shrink. In this context, accurate covariance modeling becomes essential. Our method offers a computationally tractable approach, enabling more precise and reliable inference without prohibitive computational costs, and it is already available with the data-analysis packages Enterprise [15] and Discovery [16]. We therefore advocate its adoption in future PTA investigations.

ACKNOWLEDGMENTS

We are grateful to Katerina Chatziioannou, Aaron Johnson, Javier Roulet, Bruce Allen, Joe Romano, Ken Olum, and Heling Deng for many useful discussions. M.C. is funded by the European Union under the Horizon Europe’s Marie Skłodowska-Curie project 101065440.

Appendix A: Conventions for an orthogonal reduced Fourier basis

In Fig. 4 we compare the reconstruction of a stochastic signal with the vector bases that underlie the FFTINT and SINCPhi covariance-matrix approximations. In that figure it can be seen that the two reconstructions intersect at all the nodes of the sparse time-domain basis. This would not have happened if we had used the usual conventions in the PTA literature, where the Fourier frequency spacing is set as $\Delta f = 1/T$. Furthermore, although we define the sparse time-domain basis for $t \in [2000, 6000]$, we can see that the periodicity of the signal in Figure 4 is *slightly* larger than 4000. Those two subtleties are related, and arise from the fact that in

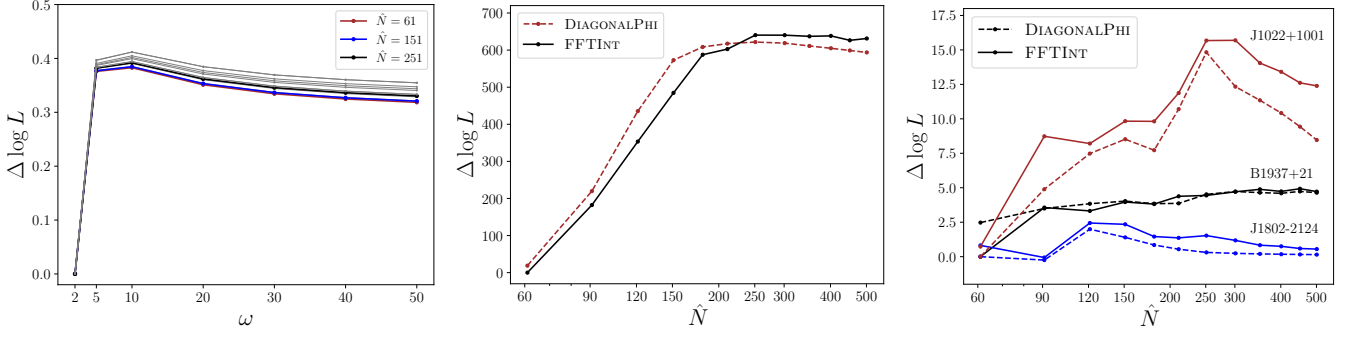


FIG. 5. Change $\Delta \log L$ in the PTA likelihood computed using FFTINT and DIAGONALPHI. **Left:** change with ω and \hat{N} , for FFTINT and the full NANOGGrav array. **Middle:** change with \hat{N} for FFTINT (with $\omega = 5$) and DIAGONALPHI for the full NANOGGrav array. **Right:** change with \hat{N} for the $\Delta \log L$ contributions of three representative pulsars.

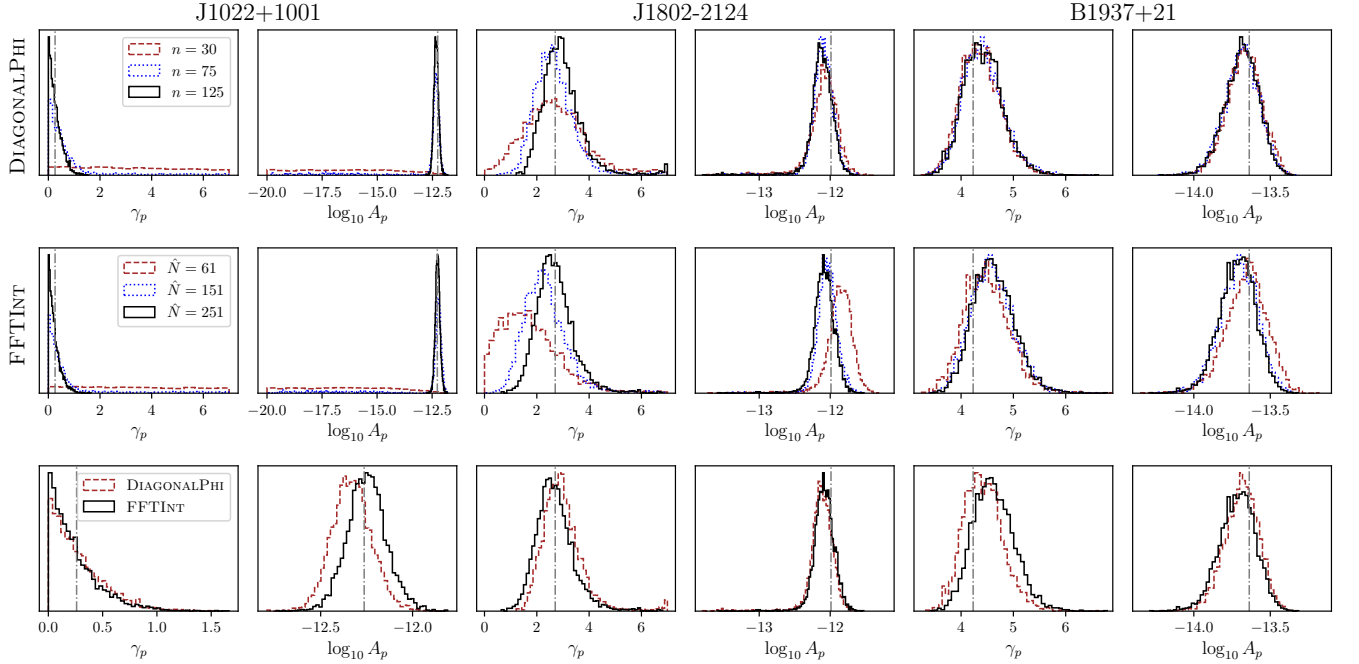


FIG. 6. Intrinsic timing-noise posteriors (γ_p and $\log_{10} A_p$) for three simulated NANOGGrav pulsars, representative of different red noise spectra. The first row shows DIAGONALPHI posteriors with $n = 30, 75, 125$, the second row FFTINT posteriors with $\hat{N} = 61, 151, 251$, and the third row compares the two methods for $\hat{N} = 251$ ($n = 125$).

the PTA literature the frequency spacing is set slightly differently from the existing literature on Fourier analysis.

We start by defining the sparse grid on $t \in [t_{\min}, t_{\max}]$, where we denote the number of nodes as \hat{N} as before. Then $t_j = t_{\min} + j\Delta t$, with $j = 0, 1, \dots, \hat{N} - 1$. On such a grid, an orthogonal Fourier basis can be constructed on the frequencies

$$f_k = k\Delta f, \quad \text{with} \quad \Delta f = \frac{1}{\hat{N}\Delta t}. \quad (\text{A1})$$

This implies that the *effective* length of the dataset is

$T_{\text{eff}} = \hat{N}\Delta t$, which is longer than the difference between the first and last observation: $t_{\max} - t_{\min} = (\hat{N} - 1)\Delta t$. In the PTA literature, the frequency spacing has traditionally been $\Delta f_{\text{trad}} = 1/T = 1/(t_{\max} - t_{\min})$, which makes the Fourier basis non-orthogonal on regularly sampled data.

The SINCPHI analyses in this manuscript are set up with the orthogonal frequency spacing of Eq. (A1). This also implies that the effective periodicity is slightly larger than $t_{\max} - t_{\min}$. An additional advantage is that the model does not require the stochastic signal to have the same response at the first and last observation.

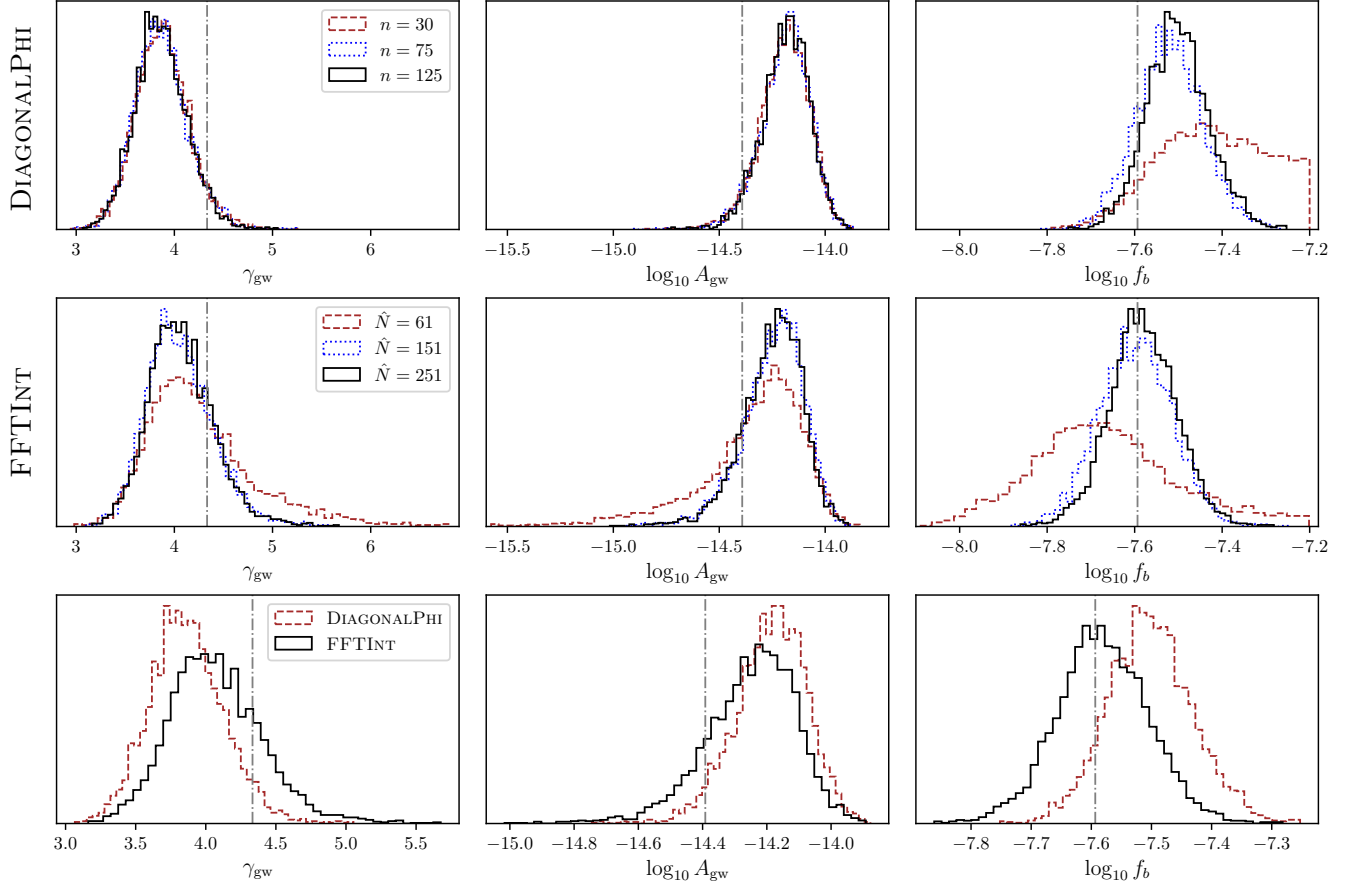


FIG. 7. Common red-noise posteriors (γ_{gw} , $\log_{10} A_{\text{gw}}$, and $\log_{10} f_b$) for the full simulated NANOGrav dataset. The first row shows DIAGONALPHI posteriors with $n = 30, 75, 125$, the second row FFTINT posteriors with $\hat{N} = 61, 151, 251$, and the third row compares the two methods for $\hat{N} = 251$ ($n = 125$).

Appendix B: Gaussian PSD stress test

The family of Gaussians parameterized with amplitude, mean, and width forms an over-complete basis in which any smooth function can be decomposed. This property of Gaussians is frequently used in many numerical applications, such as the use of Gaussian kernels in kernel density estimation. The attractive property of Gaussians for our purposes is that a Gaussian PSD has an analytical time-domain covariance function. With such an equivalence, we can set up a stress test and inspect how our method performs, which we do in this Appendix.

We define the Gaussian one-sided PSD as:

$$S(f) = \frac{2A^2}{\sqrt{2\pi}\sigma_f} \exp\left(-\frac{1}{2}\left(\frac{f - \mu_f}{\sigma_f}\right)^2\right), \quad (\text{B1})$$

where we set amplitude $A = 1$ everywhere in this Appendix, and the mean and standard deviation of the Gaussian PSD peak are respectively μ_f and σ_f . The

corresponding covariance function is:

$$C(\tau) = A^2 \exp(-2\pi^2 \sigma_f^2 \tau^2) \cos(2\pi \mu_f \tau). \quad (\text{B2})$$

In Fig. 9 we show how the various approximations presented in this paper perform on this stress test. In the legend of the top panel we have indicated what the PSD represents as a function of μ_f and σ_f : the low-frequency dominated PSDs are on the left, and the spectral lines are at the top. In the middle of the plot are features at some frequency spanning one or several bins. It is clear that the FFTINT method becomes more accurate with higher values of ω when representing spectral lines of small width. We also see that larger \hat{N} makes white (flat) spectra more accurately represented by the FFTINT method. We found the FFTINT method the most accurate approximation, but the other methods perform quite well. Visually all methods look similar in Fig. 9. Quantitatively, we see differences when comparing methods with the Gaussian PSD, similar to what we show in table I. The consistency between methods is reassuring, although subtle effects, as those in the common red-noise process, could mean that some results obtained with DIAGONALPHI on real data would be measurably corrected with FFTINT.

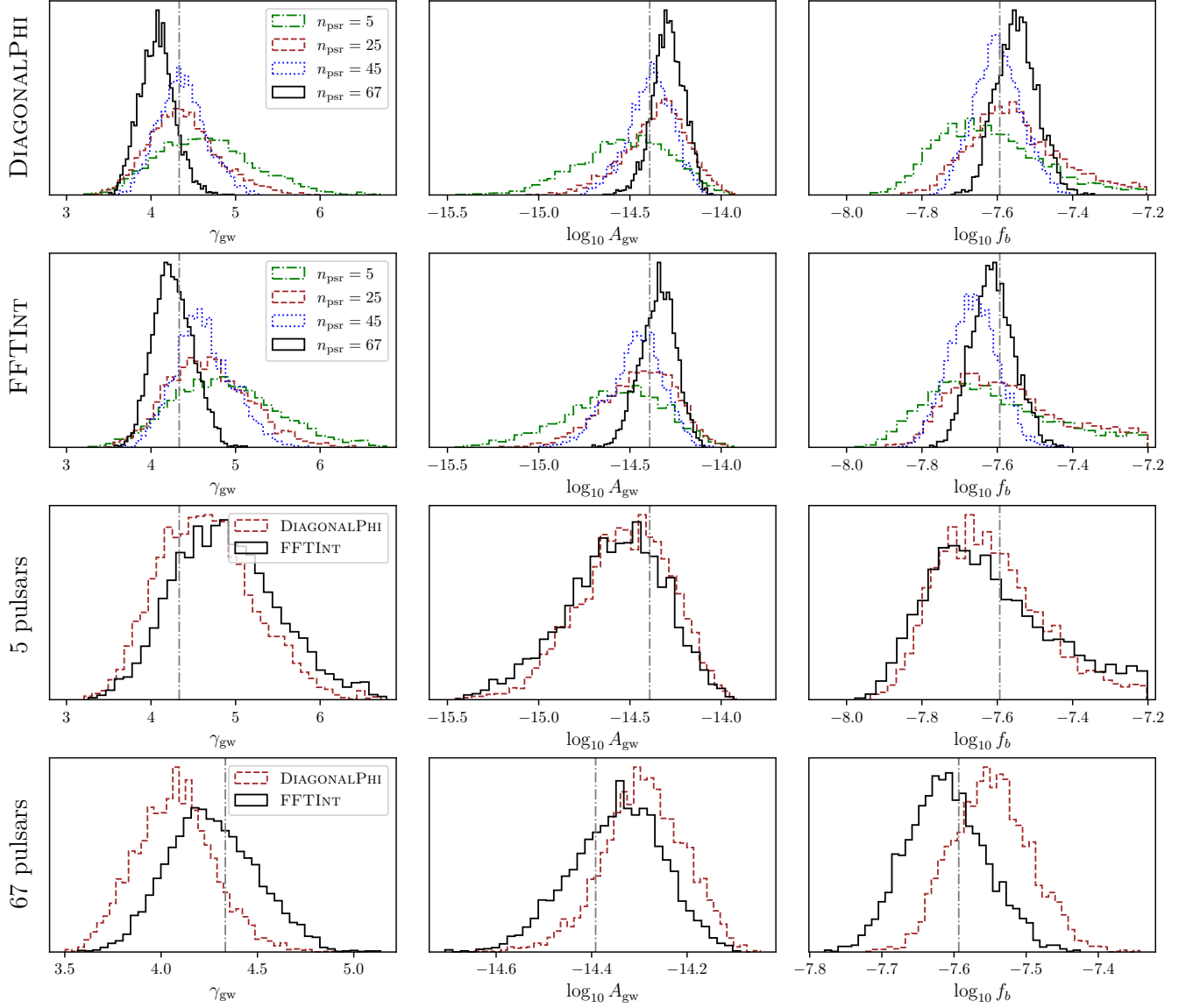


FIG. 8. Common red-noise posteriors (γ_{gw} , $\log_{10} A_{\text{gw}}$, and $\log_{10} f_b$) for a simulation without intrinsic pulsar timing noise. The first two rows show DIAGONALPHI and FFTINT for an increasing number of analyzed pulsars, while the latter two rows show a DIAGONALPHI-to-FFTINT comparison for $n_{\text{psr}} = 5$ and $n_{\text{psr}} = 67$ (the full array).

-
- [1] R. W. Romani, “Timing a millisecond pulsar array,” in *Timing Neutron Stars*, H. Ögelman and E. P. J. Heuvel, eds., pp. 113–117. Springer, 1989.
- [2] R. S. Foster and D. C. Backer, “Constructing a Pulsar Timing Array,” *Astrophys. J.* **361** (Sept., 1990) 300.
- [3] R. W. Hellings and G. S. Downs, “Upper limits on the isotropic gravitational radiation background from pulsar timing analysis,” *Astrophys. J. Lett.* **265** (Feb., 1983) L39–L42.
- [4] P. A. Rosado, A. Sesana, and J. Gair, “Expected properties of the first gravitational wave signal detected with pulsar timing arrays,” *Mon. Not. Roy. Astron. Soc.* **451** no. 3, (06, 2015) 2417–2433.
- [5] M. Anholm, S. Ballmer, J. D. E. Creighton, L. R. Price, and X. Siemens, “Optimal strategies for gravitational wave stochastic background searches in pulsar timing data,” *Phys. Rev. D* **79** no. 8, (Apr., 2009) 084030, [arXiv:0809.0701 \[gr-qc\]](#).
- [6] S. J. Chamberlin, J. D. E. Creighton, X. Siemens, P. Demorest, J. Ellis, L. R. Price, and J. D. Romano, “Time-domain implementation of the optimal cross-correlation statistic for stochastic gravitational-wave background searches in pulsar timing data,” *Phys. Rev. D* **91** no. 4, (Feb., 2015) 044048,

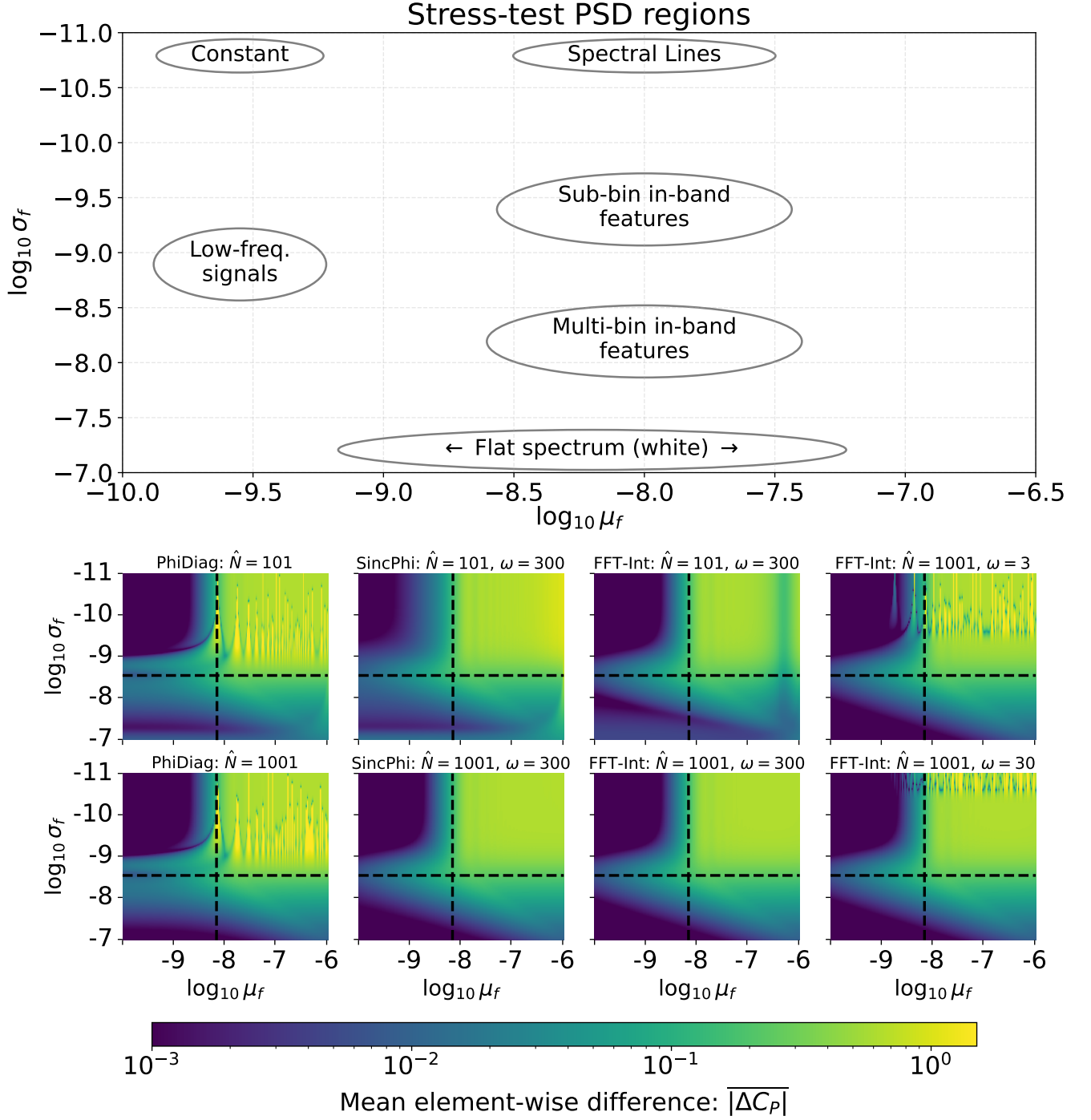


FIG. 9. Mean absolute element-wise difference $|\overline{\Delta C}|$ for various approximations of the covariance matrix. **Top panel:** legend what the PSD looks like as a function of μ_f and σ_f . **Bottom panels:** $|\overline{\Delta C}|$ as a function of μ_f and σ_f . In all plots we have placed horizontal and vertical dashed lines at $f = 1/T$.

arXiv:1410.8256 [astro-ph.IM].

- [7] S. J. Vigeland, K. Islo, S. R. Taylor, and J. A. Ellis, “Noise-marginalized optimal statistic: A robust hybrid frequentist-Bayesian statistic for the stochastic gravitational-wave background in pulsar timing arrays,”

Phys. Rev. D **98** no. 4, (Aug., 2018) 044003, arXiv:1805.12188 [astro-ph.IM].

- [8] J. D. Romano and N. J. Cornish, “Detection methods for stochastic gravitational-wave backgrounds: a unified treatment,” *Living Rev. Rel.* **20** no. 1, (2017) 2,

- arXiv:1608.06889 [gr-qc].
- [9] S. R. Taylor, *Nanohertz Gravitational Wave Astronomy*. CRC Press, Boca Raton, FL, 2021.
 - [10] R. van Haasteren and M. Vallisneri, “Low-rank approximations for large stationary covariance matrices, as used in the Bayesian and generalized-least-squares analysis of pulsar-timing data,” *Mon. Not. Roy. Astron. Soc.* **446** no. 2, (Jan., 2015) 1170–1174, arXiv:1407.6710 [astro-ph.IM].
 - [11] J. S. Hazboun, J. D. Romano, and T. L. Smith, “Realistic sensitivity curves for pulsar timing arrays,” *Phys. Rev. D* **100** no. 10, (2019) 104028, arXiv:1907.04341 [gr-qc].
 - [12] P. F. Depa, V. Domcke, G. Franciolini, and M. Pieroni, “Pulsar timing array sensitivity to anisotropies in the gravitational wave background,” arXiv:2407.14460 [astro-ph.CO].
 - [13] C. Pitrou and G. Cusin, “Mitigating cosmic variance in the Hellings-Downs curve: a Cosmic Microwave Background analogy,” arXiv:2412.12073 [gr-qc].
 - [14] R. C. Bernardo and K.-W. Ng, “Accurate pulsar timing array residual variances and correlation of the stochastic gravitational wave background,” arXiv:2409.01218 [astro-ph.CO].
 - [15] J. A. Ellis, M. Vallisneri, S. R. Taylor, and P. T. Baker, “ENTERPRISE: Enhanced Numerical Toolbox Enabling a Robust Pulsar Inference Suite,” Dec., 2019.
 - [16] M. Vallisneri *et al.*, “DISCOVERY: the next-generation pulsar-timing-array data-analysis package,” 2025. in preparation.
 - [17] J. Bradbury, R. Frostig, P. Hawkins, M. J. Johnson, C. Leary, D. Maclaurin, G. Neca, A. Paszke, J. VanderPlas, S. Wanderman-Milne, and Q. Zhang, “JAX: composable transformations of Python+NumPy programs,” 2018. <http://github.com/google/jax>.
 - [18] A. G. Baydin, B. A. Pearlmutter, A. A. Radul, and J. M. Siskind, “Automatic differentiation in machine learning: a survey,” *Journal of machine learning research* **18** no. 153, (2018) 1–43.
 - [19] M. D. Hoffman, A. Gelman, *et al.*, “The No-U-Turn sampler: adaptively setting path lengths in Hamiltonian Monte Carlo,” *J. Mach. Learn. Res.* **15** no. 1, (2014) 1593–1623.
 - [20] D. Phan, N. Pradhan, and M. Jankowiak, “Composable effects for flexible and accelerated probabilistic programming in NumPyro,” (2019) , arXiv:1912.11554.
 - [21] E. Bingham, J. P. Chen, M. Jankowiak, F. Obermeyer, N. Pradhan, T. Karaletsos, R. Singh, P. A. Szerlip, P. Horsfall, and N. D. Goodman, “Pyro: Deep universal probabilistic programming,” *J. Mach. Learn. Res.* **20** (2019) 28:1–28:6. <http://jmlr.org/papers/v20/18-403.html>.
 - [22] R. van Haasteren, Y. Levin, P. McDonald, and T. Lu, “On measuring the gravitational-wave background using Pulsar Timing Arrays,” *Mon. Not. Roy. Astron. Soc.* **395** no. 2, (May, 2009) 1005–1014, arXiv:0809.0791 [astro-ph].
 - [23] G. Agazie *et al.*, “The NANOGrav 15 yr Data Set: Observations and Timing of 68 Millisecond Pulsars,” *Astrophys. J. Lett.* **951** no. 1, (July, 2023) L9, arXiv:2306.16217 [astro-ph.HE].
 - [24] L. Lentati, P. Alexander, M. P. Hobson, S. Taylor, J. Gair, S. T. Balan, and R. van Haasteren, “Hyper-efficient model-independent Bayesian method for the analysis of pulsar timing data,” *Phys. Rev. D* **87** no. 10, (2013) 104021, arXiv:1210.3578 [astro-ph.IM].
 - [25] R. van Haasteren and Y. Levin, “Understanding and analysing time-correlated stochastic signals in pulsar timing,” *Mon. Not. Roy. Astron. Soc.* **428** (2013) 1147, arXiv:1202.5932 [astro-ph.IM].
 - [26] R. van Haasteren and M. Vallisneri, “New advances in the Gaussian-process approach to pulsar-timing data analysis,” *Phys. Rev. D* **90** no. 10, (Nov., 2014) 104012, arXiv:1407.1838 [gr-qc].
 - [27] NANOGrav Collaboration, G. Agazie *et al.*, “The NANOGrav 15 yr Data Set: Evidence for a Gravitational-wave Background,” *Astrophys. J. Lett.* **951** no. 1, (2023) L8, arXiv:2306.16213 [astro-ph.HE].
 - [28] EPTA Collaboration, J. Antoniadis *et al.*, “The second data release from the European Pulsar Timing Array III. Search for gravitational wave signals,” (6, 2023) , arXiv:2306.16214 [astro-ph.HE].
 - [29] D. J. Reardon *et al.*, “Search for an Isotropic Gravitational-wave Background with the Parkes Pulsar Timing Array,” *Astrophys. J. Lett.* **951** no. 1, (2023) L6, arXiv:2306.16215 [astro-ph.HE].
 - [30] M. T. Miles, R. M. Shannon, D. J. Reardon, M. Bailes, D. J. Champion, M. Geyer, P. Gitika, K. Grunthal, M. J. Keith, M. Kramer, and *et al.*, “The MeerKAT Pulsar Timing Array: the first search for gravitational waves with the MeerKAT radio telescope,” *Mon. Not. Roy. Astron. Soc.* **536** no. 2, (Jan., 2025) 1489–1500, arXiv:2412.01153 [astro-ph.HE].
 - [31] H. Xu *et al.*, “Searching for the Nano-Hertz Stochastic Gravitational Wave Background with the Chinese Pulsar Timing Array Data Release I,” *Res. Astron. Astrophys.* **23** no. 7, (2023) 075024, arXiv:2306.16216 [astro-ph.HE].
 - [32] J. W. Gibbs, “Fourier’s Series,” *Nature (London)* **59** no. 1522, (Dec., 1898) 200.
 - [33] H. Wilbraham, “On a certain periodic function,” *The Cambridge and Dublin Mathematical Journal* **3** (1848) 198–201.
 - [34] G. Strang, *Introduction to Applied Mathematics*. Wellesley-Cambridge Press, Wellesley, MA, 1986.
 - [35] A. D. Johnson *et al.*, “NANOGrav 15-year gravitational-wave background methods,” *Phys. Rev. D* **109** no. 10, (May, 2024) 103012, arXiv:2306.16223 [astro-ph.HE].